

Contents lists available at ScienceDirect

Materialia

journal homepage: www.elsevier.com/locate/mtla



Strength enhancement in ice-templated lithium titanate Li₄Ti₅O₁₂ materials using sucrose



Rohan Parai^a, Tessa Walters^a, Justine Marin^a, Silvina Pagola^b, Gary M. Koenig Jr.^c, Dipankar Ghosh^{a,*}

- ^a Department of Mechanical and Aerospace Engineering, Old Dominion University, Norfolk, VA 23529, USA
- Department of Chemistry & Biochemistry, Old Dominion University, Norfolk, VA 23529, USA
- ^c Department of Chemical Engineering, University of Virginia, Charlottesville, VA 22904, USA

ARTICLE INFO

Keywords: Ice-templating Li₄Ti₅O₁₂ Sucrose Microstructure Bridge density Compressive strength

ABSTRACT

Ice-templating technique enables the synthesis of novel ceramic materials with directional, anisotropic pores, and the templated structure is highly tunable. Another factor that also drives interest in ice-templated ceramics is that for a comparable level of porosity, the uniaxial compressive strength of these materials can be significantly greater in comparison to that of the conventional open-cell foams. However, the strength advantage is significantly reduced in the materials templated from low solid loading suspensions. Toward this limitation, this study sheds insights into the influence of sucrose (a water-soluble additive) and freezing front velocity (FFV) on microstructure and the uniaxial compressive response of ice-templated sintered lithium titanate (LTO, composition Li₄Ti₅O₁₂). This study used LTO as a model material. Materials were ice-templated from aqueous suspensions with 20 vol.% LTO powder and sucrose content was varied between 1-4 wt.%. The porosity of the sintered materials was in the range of 60-65 vol.%. Materials processed without sucrose exhibited lamellar morphology and low compressive strength. Sucrose had a marked influence on the connectivity between lamella walls, which significantly increased with sucrose content, and morphology became highly dendritic. The microstructural changes remarkably impacted compressive strength, which increased as high as eight-fold. Moreover, materials processed with sucrose exhibited a significant increase in strength in the continuous brittle crushing regime. By adjusting sucrose content in aqueous suspension and FFV, it is possible to synthesize ice-templated sintered LTO materials with tailored connectivity between lamella walls and harness compressive strength within a wide range of 4-80 MPa.

1. Introduction

The ice-templating technique enables the synthesis of novel ceramic materials with directional, anisotropic pores, and the templated structure is highly tunable [1–6]. The typical microstructural features of sintered ice-templated ceramics are parallel lamella walls, directional, anisotropic pores present in between the walls, and lamellar bridges that connect the walls. In the absence of lamellar bridges, morphology is lamellar, whereas the presence of a high density of bridges turns the structure dendritic. In the applications where open-cell ceramic foams are used [7–9], ice-templated ceramics have drawn significant attention because of the directional porosity in these materials. Fracture strength of open-cell ceramic foams is also essential for their successful implementation. Toward that end, another factor that also drives the interest in ice-templated ceramics is that for a comparable level of porosity, the uniaxial compressive strength of these materials can be signifi-

cantly higher in comparison to that of the conventional open-cell foams [10,11]. However, the strength advantage of ice-templated ceramics is reduced substantially in the materials that are templated from low solid loading suspensions [10].

Uniaxial compressive strength of ice-templated ceramics is strongly dependent on two key parameters: porosity and connectivity (can be referred to as lamellar bridges) between the adjacent lamella walls [5,6,12,13]. Porosity can vary significantly depending on the solid loading of suspension [6,12] and varies with particle size and sinterability of materials [6,13,14]. On the other hand, there are several parameters that can be used to tune the density of lamellar bridges [1,3,5,6,13]. Irrespective of the porosity, lamellar morphology significantly reduces the compressive strength of ice-templated ceramics [5,6,12,13]. For the compression direction parallel to the growth direction of ice crystals, lamella walls carry the applied load. The role of lamellar bridges is to anchor the walls together and prevent the walls from sliding past each other during deformation and undergo failure by buckling/bending

^{*} Corresponding author. E-mail address: dghosh@odu.edu (D. Ghosh).

[5,12,15]. Ice-templated ceramics with the lamellar morphology lack significantly in lamellar bridges (i.e., connectivity between walls) and exhibit poor compressive load-bearing capacity.

A common fabrication strategy is to template materials at higher freezing front velocity (FFV, the growth rate of solvent crystals), which causes a decrease of solvent crystal size and an increase of particle entrapment within ice crystals, both of which increase the connectivity between lamella walls and improve the compressive load-bearing capacity [5,6,13]. During the unidirectional solidification of an aqueous ceramic suspension, a particle in the suspension is either rejected or engulfed by the ice front [3,15]. The propensity of particle rejection and entrapment decreases and increases, respectively, with FFV. The rejected particles accumulate between ice lamellae and form lamella walls, whereas the entrapped particles lead to the formation of lamellar bridges between ceramic walls. With increasing FFV, as the ice crystal size decreases, pore size also decreases, which would increase pore connectivity. However, the challenge is that for the low solid loading suspensions, the effect of FFV on the templated microstructure is relatively insignificant (since most of the particles are rejected even at high FFV and materials develop with lamellar morphology) to cause any appreciable strength increase [5,6,12,13]. Ice-templated ceramics are typically fabricated from submicrometer size particles. It has been shown that particles of greater size can promote particle entrapment during the templating step and enhance lamellar bridge density [5,6,13]; however, poor sinterability of large ceramic particles can offset the effect of increased wall connectivity [5,13]. Moreover, ceramic powder materials of various particle sizes may not be readily available.

Soluble additives can impact the growth kinetics and morphology of ice crystals, and therefore, pore size and connectivity between lamella walls in ice-templated ceramics. Porter et al. [16] studied the influence of polyethylene glycol (PEG) and the corresponding changes in suspension viscosity. They showed that smaller pore areas and aspect ratios enhanced the strength of ice-templated titania (TiO2). Ice-templated materials were developed from 10 vol.% TiO2 suspensions, and the porosity of the sintered materials was about 80 vol.%. However, the strength improvement was only marginal, in the range of 3-7 MPa. Also, since PEG increases the viscosity of ceramic suspensions, the use of PEG for higher solid loading suspensions may not be feasible. Munch et al. [17] studied the effects of sucrose on pore architecture and the strength of icetemplated alumina (Al2O3) materials. Their study revealed that the use of 4 wt.% sucrose promoted lamellar structure with significant microscopic roughness on the lamella walls. Whereas, use of 10 wt.% with adjusting pH to 2.5 by using citric acid resulted in a cellular structure with very smooth lamella walls, reduced pore size, and increased wall connectivity compared to the materials processed with 4 wt.% sucrose. The decrease in pore size also increased the compressive strength of the materials approximately from 6 MPa to 12 MPa. Although the study by Munch et al. [17] lacks a systematic investigation of the effects of sucrose, their findings suggest that sucrose can be utilized in tailoring ice-templated microstructure and strength.

Therefore, the purpose of this study is to conduct a systematic investigation and shed insights into the influence of sucrose content in low solid loading (20 vol.%) aqueous lithium titanate (LTO, chemical composition Li4Ti5O12) suspensions on ice-templated sintered microstructure and structure-mechanical property relationships. LTO is an established anode material for lithium (Li)-ion batteries [18]. Recently, few studies implemented the ice-templating technique for processing Li-based porous electrodes for Li-ion batteries [19,20]. Although these studies reported promising electrochemical performance, there is a lack of attention on the mechanical behavior and structure-mechanical property relationships of Li-ion based ice-templated sintered electrodes, which is equally essential to fully realize the potential of directional porosity for Li-ion batteries. Also, there is no study reported in the open literature on the fabrication of porous LTO materials using the ice-templating technique. Thus, this study explicitly focuses on the fabrication, characterization of compressive mechanical properties, and process-structure-mechanical property relationships in ice-templated sintered LTO materials. The electrochemical performance of these materials with the variation of the microstructure is well beyond the scope of this work and will be addressed in a separate investigation.

To develop ice-templated LTO materials, it is necessary to understand the role of processing variables to achieve control over different length-scales of the templated structure and the relationship between microstructure and strength. Here, we studied the combined effects of sucrose content in aqueous LTO suspensions and FFV to understand the tunability of ice-templated microstructure and compressive strength. In all the aqueous suspensions used in this work, LTO powder content was 20 vol.%. Materials were developed from four different compositions of aqueous LTO suspensions. One composition contained 20 vol.% LTO but no sucrose. Whereas, the three other compositions, in addition to 20 vol.% LTO, contained 1, 3, and 4 wt.% (with respect to water content in suspension) sucrose. For each composition, ice-templated materials were fabricated at both relatively high ($\sim 30 \,\mu\text{m/s}$) and low ($\sim 20 \,\mu\text{m/s}$) FFVs. The templated materials were freeze-dried and then sintered at 950 °C. A scanning electron microscope (SEM) was used for microstructure analysis. The mechanical response of sintered LTO materials was investigated under uniaxial compressive loading conditions. Our findings revealed that a remarkable strength gain could be achieved by developing ice-templated ceramics with sucrose without affecting porosity. By adjusting sucrose content in aqueous suspension and FFV during the templating step, it is possible to synthesize ice-templated sintered LTO materials with tailored connectivity between lamella walls and hamess compressive strength within a wide range of 4-80 MPa. The methods and results are equally applicable to other ceramic materials as well.

2. Experimental

2.1. As-received LTO powder, two-step sieving, and preparation of aqueous suspensions

In this work, ice-templated porous materials were fabricated using commercially available LTO powder (NANOMYTE® BE-10, NEI Corporation, Somerset, NJ, purity > 98%). Note that detailed electrochemical and materials characterization of this material is outside of the scope of this study; however, this information can be found in previous reports [21,22]. Figs. 1a and 1b show SEM images at low and high magnifications, respectively, of the as-received LTO powder. SEM image in Fig. 1a reveals that the as-received powder contains agglomerates with few agglomerates as large as 80 μ m, and Fig. 1b reveals that LTO particles are ultrafine with individual particles appear to be below 500 nm. We performed a two-step sieving process to break the agglomerates in the as-received powder. First, the as-received LTO powder was mixed with deionized (DI) water (in the proportion of mass ratio of 1:1.2) and yttriastabilized zirconia (YSZ, 5 mm diameter, Inframat® Advanced Materials LLC) milling media in a Nalgene bottle, with the ceramic powder to milling media mass ratio of 1:4. Next, aqueous LTO suspensions were milled using a jar mill for 6 h and sieved through a 325 mesh (equivalent to 45 µm) to separate from the zirconia (ZrO2) spheres. Next, LTO suspensions were placed inside an oven at a temperature of 125 °C to evaporate water slowly. The dried LTO powder was sieved again using the same mesh size sieve. Fig. 1c shows an SEM image of the LTO powder obtained after the two-step sieving process, and we can observe that the dried LTO powder was relatively free of agglomerates.

Ice-templated LTO materials were fabricated from four different compositions. One composition is without sucrose, which we refer to here as LTO-0. Three other compositions contained 1 wt.% (referred to here as LTO-1), 3 wt.% (referred to here as LTO-3), and 4 wt.% (referred to here as LTO-4) sucrose, with respect to water content in suspensions. For all the compositions, LTO content in suspensions was 20 vol.%. For LTO-0 composition, aqueous suspensions were prepared by mixing LTO powder with DI water that contained cetyl trimethyl ammonium bromide (CTAB, cationic dispersant). The CTAB concentration used was

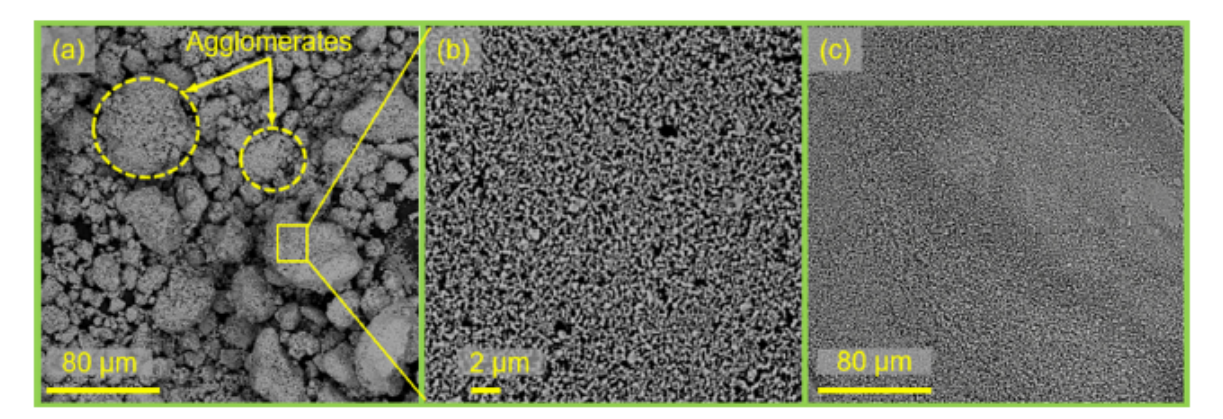


Fig. 1. (a), (b) SEM images of as-received LTO powder at different magnifications. The as-received LTO powder is highly agglomerated with some agglomerates larger than 100 μm and the high-magnification SEM image (Fig. 1b) reveals ultrafine LTO particles (< 500 nm). (c) shows SEM image of LTO powder obtained after the two-step sieving process (discussed in Section 2.1), revealing the absence of large agglomerates.

0.02 g/cc with respect to the total volume of DI water in suspension. For this composition (without sucrose), our preliminary studies revealed the significant difficulty of mixing LTO powder with the required amount of DI water (to prepare 20 vol.% suspension) without using CTAB. Without CTAB, the suspensions became highly viscous during milling. For these suspensions with CTAB, we also observed slight foaming at the end of milling. To remove the foams present in the suspension, an antifoaming agent (SURFYNOL®104 PG 50), in the proportion of 0.3 wt.% of LTO powder, was added. Interestingly, the presence of sucrose in DI water enabled the mixing of LTO powder with water without the need for using CTAB. We also did not observe any foaming in the suspensions containing sucrose. For milling, ZrO2 milling media to ceramic powder ratio was 1:4. Each suspension was milled for 1 h at an RPM of about 30. Binder solution was next added, and the suspensions were milled for another hour but at a reduced rpm. The binder solution was prepared by dissolving poly(2-ethyl-2-oxazoline) in DI water (2.5 times of binder mass) and was added to the ceramic suspensions as such the binder amount was 4 wt.% of LTO powder. Each suspension next was passed through a 325 mesh (45 µm) to separate the ZrO2 media, and after this stage, the suspensions were ready for ice-templating.

2.2. Ice-templating of aqueous LTO suspensions

All the aqueous LTO suspensions were ice-templated following the same steps. In this work, we utilized a custom-made device for the ice-templating process. Details for the custom-made device, including a schematic, can be found elsewhere [23]. In this methodology, first, a Teflon tube (mold) is placed on a thin copper (Cu) plate (referred to here as "Cold-finger"), and next filled with an aqueous ceramic suspension. The suspension in the mold is then unidirectionally frozen. For this purpose, the entire assembly is inserted inside liquid nitrogen (N2) Dewar but placed above the liquid N2. The temperature of Cold-finger reaches below 0°C, and ice crystals nucleate at the bottom of suspension in contact with Cold-finger and grow upward under the influence of the thermal gradient. By adjusting the gap between the Cold-finger and liquid N2, we can control the unidirectional freezing front velocity (FFV, growth rate). In this work, we used a Teflon tube of an inner diameter of 16 mm and a height of 25 mm, with a final target height for the sintered samples of approximately 8 mm. The samples were ice-templated at two different gaps between the Cold-finger and liquid N2, which allowed the use of both relatively high and low FFVs. The average FFV for each sample was determined by dividing the height of a frozen sample with the time required for completion of the solidification of the suspension [5,24]. From each batch of LTO suspension and at each FFV regime, four samples were fabricated. The frozen samples were freeze-dried at a pressure of 0.014 mbar and temperature of -50 °C inside a freeze dryer (2.5 L, Labconco, Kansas City, Missouri) for 96 h. The freeze-dried samples without sucrose were heated from room temperature to 450 °C at a ramp rate of 5 °C/min and held for 4 h for binder burnout. Next, samples were heated to 950 °C using a ramp rate of 2 °C/min and sintered for 2 h. For the samples with sucrose, a slightly modified heating schedule was utilized, although the highest temperature and the hold at the highest temperature were the same. From room temperature to 195 °C at a ramp rate of 5 °C/min and held for 1 h, from 195 °C to 220 °C at a ramp rate of 1 °C/min and held for 1 h, from 220 °C to 450 °C at a ramp rate of 2 °C/min and held for 3 h, from 450 °C to 950 °C using a ramp rate of 2 °C/min and sintered for 2 h. All the sintered samples were cooled from 950 °C to 450 °C at a ramp rate of 2 °C/min and from 450 °C to room temperature at a ramp rate of 5 °C/min. Sintering was performed in a tube furnace (NBD, T-1700-60IT). The heating schedule utilized for the samples with sucrose was selected based on the study by Kumar et al. [25] on thermal decomposition and burnout behavior of sucrose.

2.3. Characterization of ice-templated sintered LTO materials

All the sintered LTO samples were of cylinder form with diameter and height of approximately 13 mm and 7 mm, respectively. X-ray diffraction (XRD) patterns of the as-received LTO powder and sintered LTO material were collected to confirm that the structure of the material was not changed during high temperature processing. XRD data were collected using a benchtop D2 Phaser (Bruker AXS) powder diffractometer with Cu Kα radiation and a LynxEye position-sensitive detector, working in linear mode with 2.0° opening, in Bragg-Brentano configuration and reflection geometry. The specimens were loaded onto Si lowbackground flat plate sample holders (1.5 cm diameter x 0.5 mm depth) and spun at 15 rpm. Two 2.5° soller slits were placed in the incident and diffracted beams, respectively. A 0.6 mm divergence slit was used in the incident beam, and a 3 mm detector slit and a Ni filter were placed in the diffracted beam. 2θ was scanned from 10° to 100° in 0.02° steps, with 1.5 s counting time/step. The lattice parameters from the diffraction data were evaluated by FULLPROF software [38].

From each sintered cylinder sample, one disk specimen of 3 mm thickness was extracted using a diamond saw at a height 2 mm from the bottom, see schematic in Fig. 2. The extracted disk specimens were used to characterize porosity, microstructure, and uniaxial compressive mechanical response. The density of each sintered disk (ρ^*) was determined from the measurements of mass and dimensions, whereas relative density (ρ_r) was calculated as $\rho_r = \rho^*/\rho_s$, taking bulk density ρ_s of LTO as 3.47 g/cm³. Total porosity was estimated as $p_t = (1-\rho_r) \times 100$. The microstructure of sintered LTO materials was characterized using a desktop SEM (Phenom Pure), and SEM images were obtained from cross-sectional planes perpendicular to the growth direction of ice crystals. The schematic shown in Fig. 2 illustrates the cross-sectional planes referred to as top and bottom planes, perpendicular to the ice-growth di-

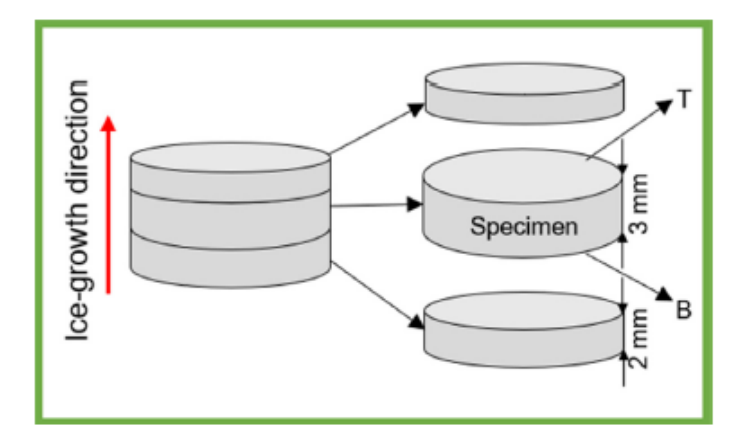


Fig. 2. Schematic showing location in sintered cylinder from where a thin disk was extracted for characterization. T and B represent top and bottom planes, respectively, from where SEM images were obtained for microstructure analysis.

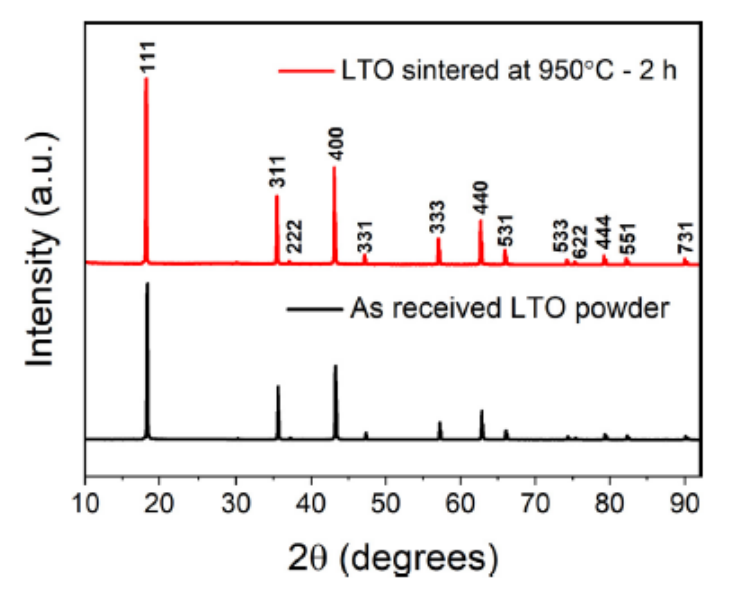


Fig. 3. Overlay of the XRD patterns of as-received LTO powder and icetemplated sintered LTO material (at 950 °C for 2 h). The Miller indices corresponding to each diffraction peak are also shown. Peaks were assigned based on the $Fd\bar{3}m$ space group.

rection, from where SEM images were obtained for microstructure analysis. As indicated in the schematic, the distance between the top and bottom planes is about 3 mm. From the SEM images, lamella wall thickness, wavelength, pore size, pore area, and lamellar bridge density were estimated. For each composition, FFV, and image plane, we utilized two SEM images for microstructure analysis. Mechanical response of sintered LTO disks was investigated under uniaxial compressive loading conditions employing a mechanical testing machine (Tinius Olsen 10ST). The compressive load was applied parallel to the ice-growth direction.

3. Results

3.1. Phase purity of as-received LTO powder and sintered LTO material

Fig. 3 shows the XRD patterns of the as-received LTO powder and sintered LTO material. The diffraction patterns of both materials are in close agreement with that of the impurity-free LTO cubic spinel structure, with Fd3m space group symmetry (JCPDS card #49-0207) and Z=8 [26]. The lattice parameters are 8.3595 Å and 8.3606 Å for the commercial powder and the sintered material, respectively, very close to previously reported values for $Li_4Ti_5O_{12}$ (a = 8.352 Å, V = 583.6 Å³

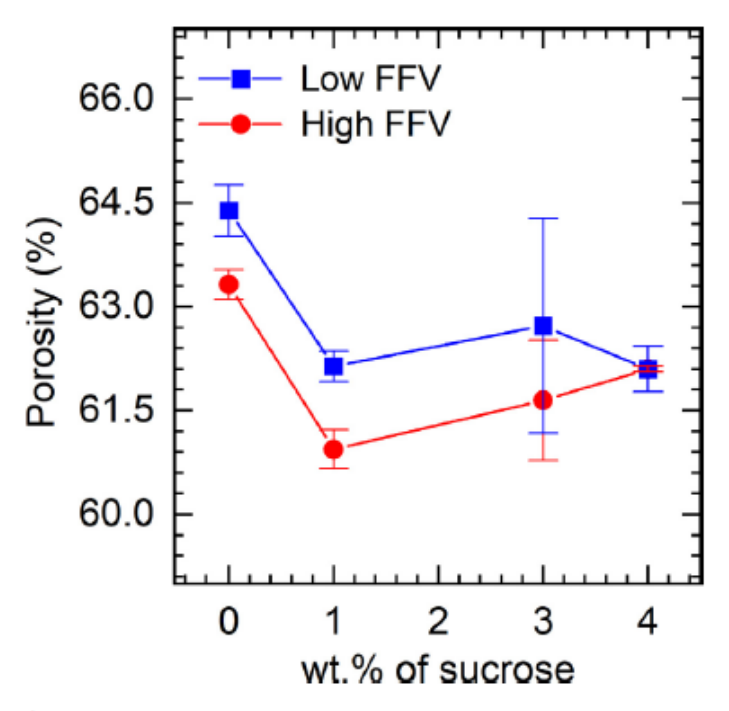


Fig. 4. Variation of porosity (p_t) in sintered LTO samples processed at relatively high FFV (\sim 30 μ m/s, red circles) and low FFV (\sim 20 μ m/s, blue squares) with sucrose content. The error represents the standard deviation of 4 independent samples.

[18]). No evidence of any impurity phases, such as rutile or anatase ${\rm TiO_2}$, was observed in the diffraction data. Hence, Fig. 3 confirms phase purity in the as-received powder and that sintering at 950° C did not affect the crystal structure of LTO.

3.2. Effects of sucrose and FFV on porosity

Fig. 4 shows the variation of total porosity in the ice-templated sintered LTO materials as a function of sucrose content. Table 1 lists the average FFV and porosity values. In a given FFV regime (high or low), all the materials were processed at comparable FFV. The range across all "low FFV" samples was 22 to 24 µm/s, and across all "high FFV" samples was 31 to 35 μ m/s. For each composition, the porosity of the materials processed at relatively high FFV is slightly lower compared to the materials processed at relatively low FFV. Similarly, the porosity of the materials fabricated with sucrose is about 2 vol.% lower than the materials processed without sucrose. Thus, the change in sucrose content in aqueous LTO suspensions did not cause any significant variation in total porosity. Typically, the porosity of sintered ice-templated ceramics developed from 20 vol.% aqueous suspensions is about 70 vol.% [12], whereas porosity of sintered LTO materials is observed to be in the range of 60-65 vol.%. The lower porosity could be attributed to the ultrafine size of LTO particles since it is known that a decrease of particle size promotes sinterability. Further, the reduction in porosity in the LTO materials fabricated with sucrose can be related to relatively smaller pore sizes in these materials compared to LTO-0 materials, which favor densification during sintering [5,24], discussed further in the next

Recall that to prepare aqueous suspensions for ice-templating for the LTO-0 composition, dispersant and antifoaming agent was utilized. Whereas, the sucrose-containing LTO suspensions were prepared without dispersant and antifoaming agent. Fig. 4 suggests only a moderate porosity difference (approximately 2 vol.%) between sintered LTO materials prepared from suspensions with and without CTAB. Microstructural investigation (Section 3.3) did not reveal any agglomerates in the sintered materials corresponding to sucrose-containing compositions. Thus, it was challenging to prepare aqueous suspensions of the commer-

Table 1
Variation of porosity in the ice-templated sintered LTO materials processed at relatively high and low freezing front velocities (FFVs) with sucrose content in aqueous LTO suspensions. The error represents the standard deviation of a minimum of 4 independent samples.

| Sucrose content (wt.%) /Composition ID | High FFV | | Low FFV | |
|--|---|--|--|--|
| | FFV (µm/s) | Porosity (vol. %) | FFV (µm/s) | Porosity (vol. %) |
| 0 (LTO-0) 1 (LTO-1) 3 (LTO-3) 4 (LTO-4) | 34.3 ± 0.6 32.2 ± 0.01 32.6 ± 0.9 32.4 ± 1.2 | 63,3 ± 0,2 60,9 ± 0,3 61,7 ± 0,9 62,1 ± 0,1 | 23.1 ± 0.8 23.4 ± 0.6 22.4 ± 0.4 22.5 ± 0.1 | 64.4 ± 0.4 62.1 ± 0.2 62.7 ± 1.6 62.1 ± 0.3 |

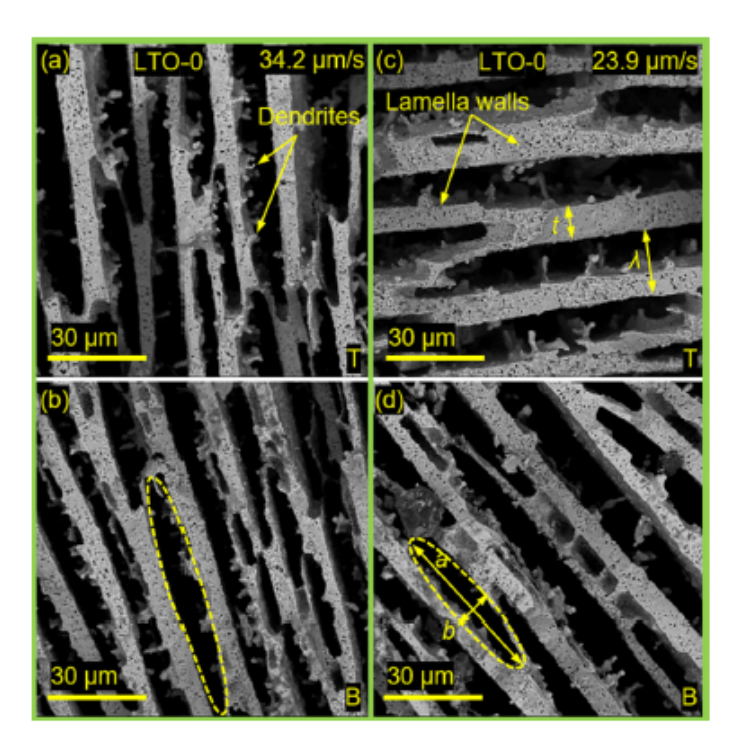


Fig. 5. Representative high-magnification SEM images revealing ice-templated microstructure of sintered LTO-0 materials processed at relatively high FFV (a-b) and low FFV (c-d). T or B shown in each SEM image (bottom right corner) corresponds to either top image plane or bottom image plane, respectively (refer to Fig. 2). Low-magnification SEM images are provided in the Supplementary material, Fig. S1.

cially available LTO powder used in this work and required the addition of dispersant and antifoaming agent. Alternatively, aqueous LTO suspensions were also prepared without dispersant and antifoaming agent by using sucrose. The absence of agglomerates in the sintered materials suggests the effectiveness of sucrose in uniformly dispersing LTO particles in aqueous media without using a dispersant.

3.3. Effects of sucrose and FFV on ice-templated microstructure

Fig. 5 shows representative high-magnification SEM images of sintered LTO-0 materials processed at relatively high (34.2 μ m/s) and low (23.9 μ m/s) FFVs and for both top (T) and bottom (B) image planes. Low-magnification images are provided in Fig. S1 (Supplementary material). For both high and low FFVs, we can observe the characteristic features of ice-templated ceramics such as parallel lamella walls and large, elongated macropores (referred to as inter-lamellar pores), which are observed in ice-templated materials processed from low solid loading suspensions [6,12,24]. A few of those pores are indicated on the SEM images by yellow dashed ellipses (Figs. 5b, 5d). In fact, many of the pores are too long (on the image plane), and the SEM images captured part of the pores only. SEM images reveal the presence of micropores in lamella walls as well. For both FFV regimes, lamella wall

thickness is higher on the top plane compared to the bottom plane, suggesting an increase in thickness along the growth direction of ice crystals. Whereas, with the increase in FFV, wall thickness decreased. During the ice-templating process, as the crystals grow upward under the influence of unidirectional temperature gradient, the solidification front continues to decelerate due to the need for the heat to be transferred to the freezing surface (Cold-finger) through an increasing amount of solid (frozen) material. Growth of the ice crystals that are more favorably aligned with the freezing direction dominates over the others [27]. As a result, in due course of crystal growth, the microstructure coarsens with increasing distance from the freezing surface, and the average thickness of ice lamellae increases. The result is that in the sintered materials, we observe a gradual increase in the average lamella wall thickness along the growth direction of ice crystals [6]. On the other hand, an increase in the unidirectional temperature gradient (increasing FFV) enhances the number of ice crystals that nucleate. As a result, at high FFVs, a greater number of ice crystals develop that are relatively thinner than low FFVs where a smaller number of ice crystals develop that are relatively thicker [3]. As a result, with increasing FFV thickness of lamella walls decreases [5,6,24]. The morphology of the LTO-0 materials is highly lamellar due to a lack of lamellar bridges (connectivity between lamella walls). We can also observe a significant presence of ceramic dendrites on the surfaces of lamella walls, which resulted from the growth of secondary ice dendrites on the surfaces of primary ice crystals (primary dendrites) during the solidification step [27].

Fig. 6 shows representative high-magnification SEM images of sintered LTO materials, which were fabricated from the suspensions containing sucrose at relatively high FFVs (~30 µm/s) for both top (T) and bottom (B) image planes. Low-magnification images are provided in Fig. S2 (Supplementary material). A drastic effect of sucrose on icetemplated microstructure can be observed, particularly with higher sucrose content (LTO-3 and LTO-4). In these materials, the primary effect of sucrose is the significant increase in connectivity between the lamella walls. The templated microstructures in the LTO-1, LTO-3, and LTO-4 are also observed to be more heterogeneous. It appears that with the increase in sucrose content in LTO suspensions, pore major axis and thus wall connectivity decreased and increased, respectively. Due to the increased connectivity between adjacent lamella walls, pore morphology changed from being highly lamellar in the LTO-0 materials to dendritic in the LTO-4 materials. Fig. 7 shows representative high-magnification SEM images of sintered LTO materials with varying sucrose content, which were fabricated at relatively low FFVs (~20 μm/s) for both top (T) and bottom (B) image planes. Low-magnification images are provided in Fig. S3 (Supplementary material). These materials exhibited microstructural features that are observed to be similar to those of the high FFV materials. For each sucrose-containing composition, the overall pore morphology is similar across the FFV regimes. Recall that porosity of all the materials is within a narrow range of 60-65 vol.%, and the addition of sucrose LTO suspensions only decreased porosity in the sintered materials by 2 vol.%. Mass transport during sintering is influenced by the radius of curvature of the solid-vapor interface, and the density of sintered foams increases with a decrease of the pore radius of curvature [5,24,28]. Since the pore radius of curvature decreases with pore size,

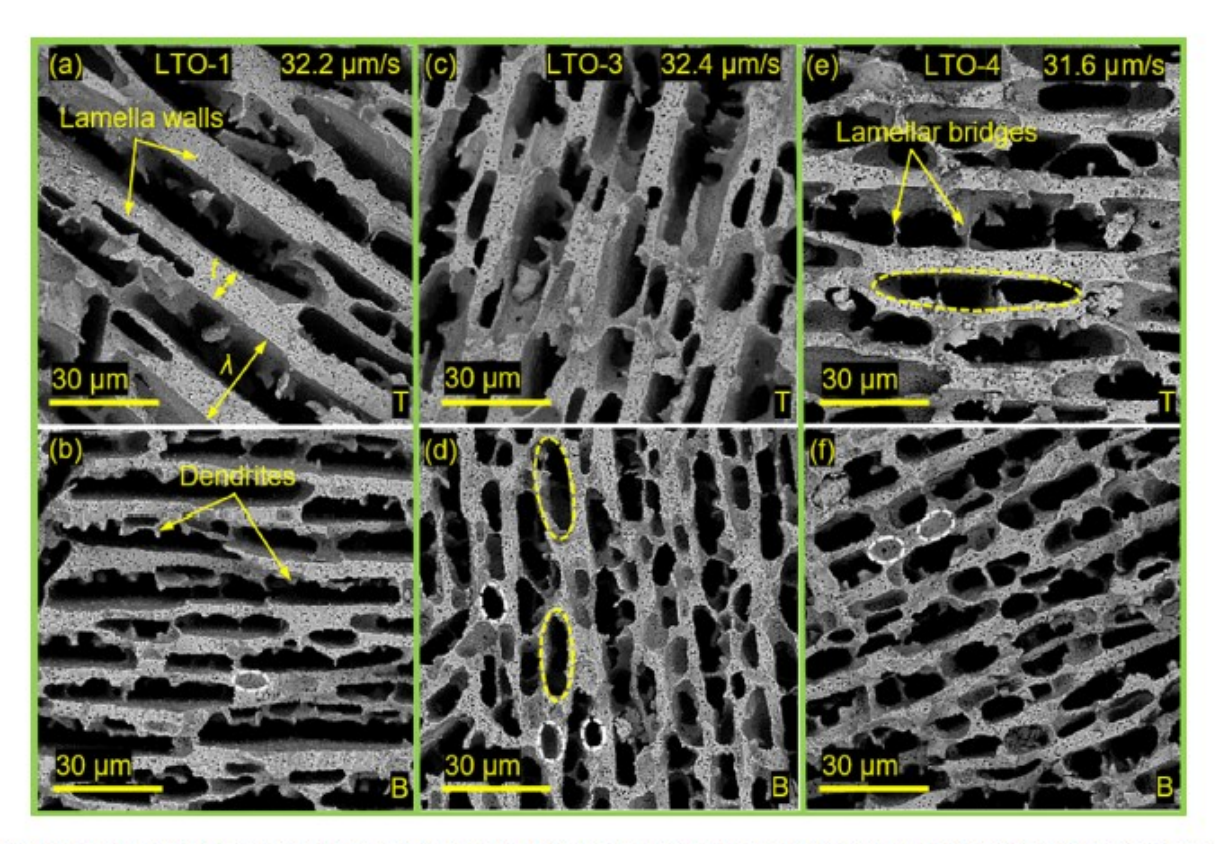


Fig. 6. High-magnification SEM images of ice-templated LTO materials processed at relatively high FFV: (a-b) LTO-1, (c-d) LTO-3, (e-f) LTO-4. T or B shown in each SEM image (bottom right corner) corresponds to either top image plane or bottom image plane, respectively (refer to Fig. 2). Low-magnification SEM images are provided in the Supplementary material, Fig. S2.

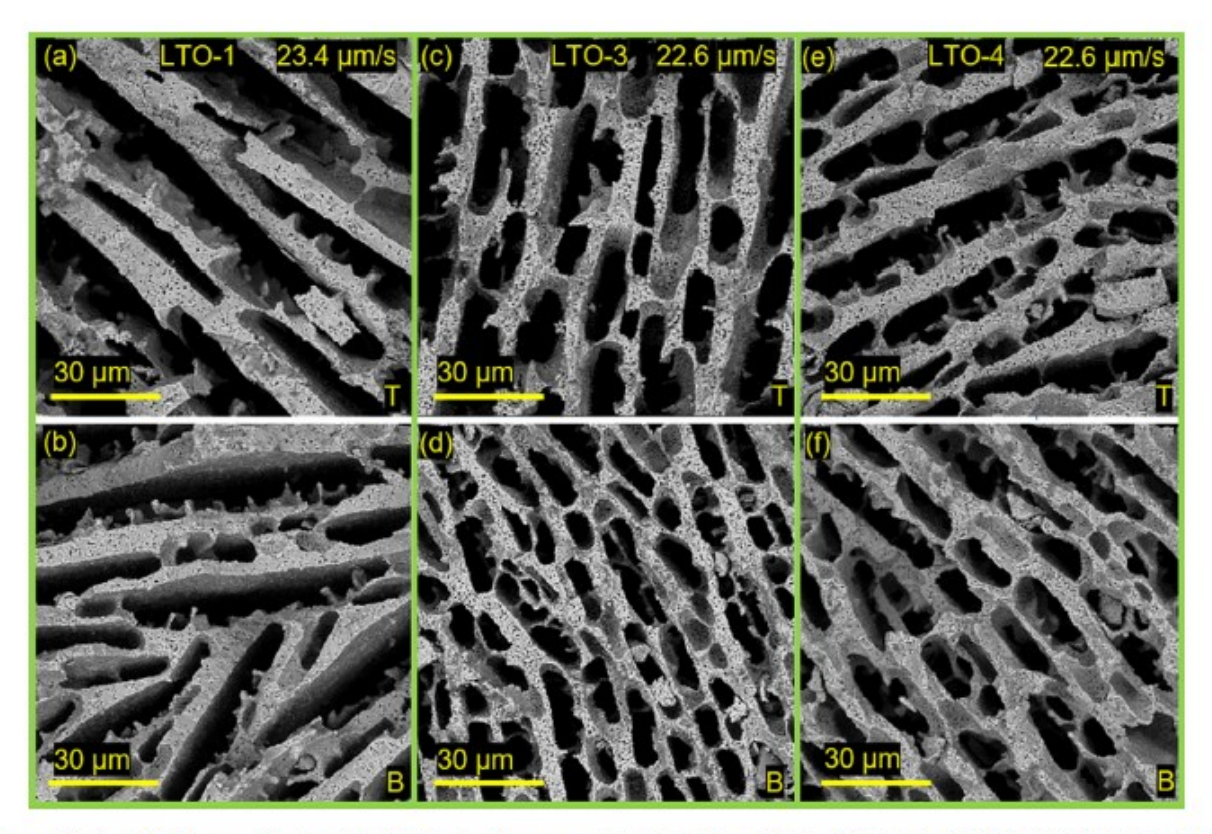


Fig. 7. High-magnification SEM images of ice-templated LTO materials processed at relatively low FFV: (a-b) LTO-1, (c-d) LTO-3, (e-f) LTO-4. T or B shown in each SEM image (bottom right corner) corresponds to either top image plane or bottom image plane, respectively (refer to Fig. 2). Low-magnification SEM images are provided in the Supplementary material, Fig. S3.

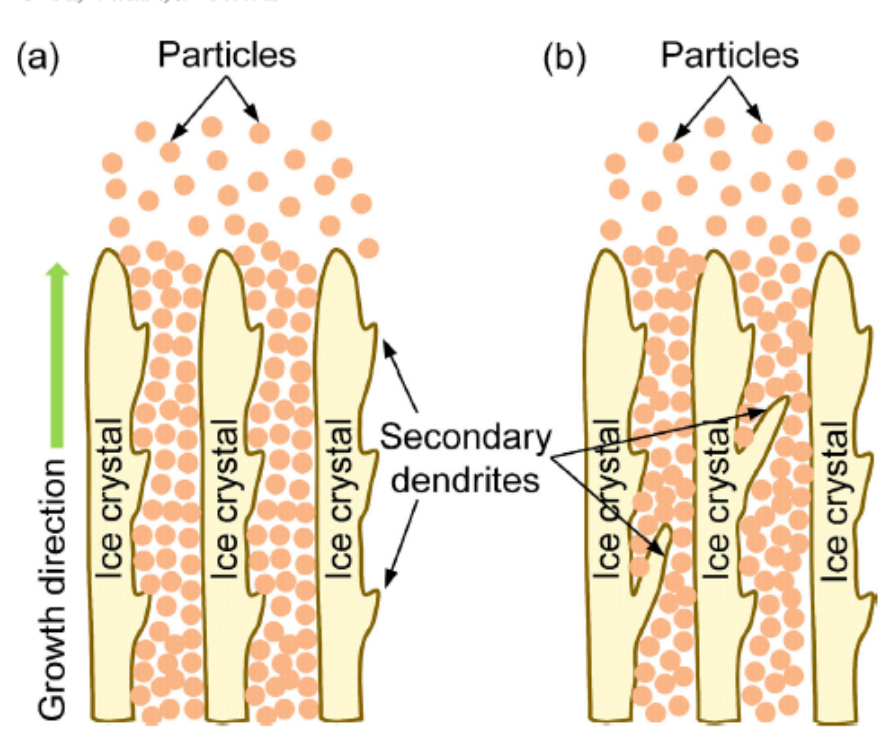


Fig. 8. Simplified schematics showing growth of (a) primary ice dendrites, representative of LTO-0 materials, and (b) both primary and secondary ice dendrites, representative of LTO-1, LTO-3 and LTO-4 materials. Removal (through freezedrying) of primary ice dendrites results in inter-lamellar pores, whereas removal of secondary dendrites can result in intralamellar pores.

the decrease in porosity in the materials fabricated with sucrose can be attributed to enhanced mass transport during sintering.

In the LTO-1 (Fig. 6b), LTO-3 (Fig. 6d), and LTO-4 (Fig. 6f) materials, many of the pores adjacent to the inter-lamellar pores are relatively equiaxed, as shown by the white dashed ellipses/circles. Thus, two sets of pores can be identified in the microstructure of LTO materials, templated from aqueous suspensions containing sucrose. One set consists of the typical inter-lamellar pores that are continuous through the growth direction of ice crystals, and these pores correspond to the regions that were occupied by the primary ice dendrites [29]. On the other hand, the second set of pores are most likely not through along the growth direction (see pores shown in Fig. 6b (B) and Fig. 6f (B)), and could correspond to the regions that were occupied by the secondary ice dendrites that significantly branched out from the primary ones [28],[30]. We can refer to these pores as intra-lamellar pores, which typically evolve in icetemplated ceramics that are processed with additives and/or from high solid loading suspensions. A separate study will be conducted to investigate the pore characteristics in the ice-templated LTO materials using X-ray tomography. A point to be made here that due to the porous nature of lamella walls, the intra-lamellar pores can also be accessed by a fluid.

In Fig. 8, we have shown simplified schematics to illustrate the formation of pores from primary and secondary ice dendrites. During the unidirectional solidification of low solid loading aqueous ceramic suspensions, primary ice lamellae that develop are continuous along the growth direction. Typically, one side of the ice lamellae contains small dendritic arms that terminate at the boundary of particles which have been rejected by the growing ice crystals and accumulated between primary dendrites [27-29], as schematically shown in Fig. 8a. Upon freezedrying, sublimation of these ice crystals will result in pores that will be continuous along the growth direction (inter-lamellar pores). The presence of water-soluble additives such as polyvinyl alcohol (PVA) and PEG in aqueous ceramic suspensions has shown to cause significant growth of some of the secondary ice dendrites during the solidification process, and pore morphology in the ice-templated materials becomes dendritic with increased wall connectivity [30,31]. Fig. 8b shows a highly simplified schematic, which illustrates a few secondary ice dendrites that have grown extensively. Sublimation of primary and secondary ice dendrites will result in both continuous and local pores. Pekor et al. [30,31] showed that when PVA or PEG was added to aqueous alumina (Al_2O_3) ceramic suspensions, approximately equiaxed pores developed adjacent to large lamellar pores, similar to the pore characteristics observed in the LTO-1, LTO-3, and LTO-4 materials. It is possible that sucrose (watersoluble additive) also promoted the growth of secondary ice dendrites and resulted in the development of local pores. The overall effect is a significant increase in wall connectivity.

Finally, we show the microstructures of lamella walls. Fig. 9 shows SEM images at three different magnifications, comparing the characteristics of lamella walls of sintered LTO-0 (a-c) and LTO-4 (d-f) materials. Note that the image plane here is parallel to the growth direction of ice crystals. All the images reveal the porous nature of lamella walls. While we can observe the presence of dendrites on the surfaces of lamella walls of both materials, they appear to be more periodic, well developed, and running across a longer length in the LTO-4 materials.

3.4. Estimation of microstructural parameters

Fig. 10 shows the variation of average lamella wall thickness (t), pore minor axis (b), and pore major axis (a) with sucrose content for both high and low FFV regimes. See Fig. S4 (Supplemental material) for the variation of wavelength, λ, and pore area. High standard deviations make it challenging to understand the exact trend in the data and indicate the heterogeneous nature of templated microstructure. In general, for each composition, with the increase in FFV lamella wall thickness decreased. In each FFV regime, lamella wall thickness decreased with sucrose content. In each material, the average values of the measured parameters are higher on the top plane compared to the bottom plane, which suggests an increase in wall thickness and spacing along the growth direction of ice crystals. With the increasing sucrose content, a decrease in wall thickness is consistent with the increase in wall connectivity. Across all the compositions, the mass of LTO particles is constant in the suspensions. With increasing sucrose content, as more LTO particles developed connections between lamella walls, a lesser number of particles were available for the formation of walls, and hence wall thickness decreased. Fig. 10b suggests the insignificant effect of sucrose on pore minor axis (which can be considered as equivalent to the width of ice crystals). Whereas, Fig. 10c reveals a sharp decrease in pore major axis with increasing sucrose content, which is also an indication

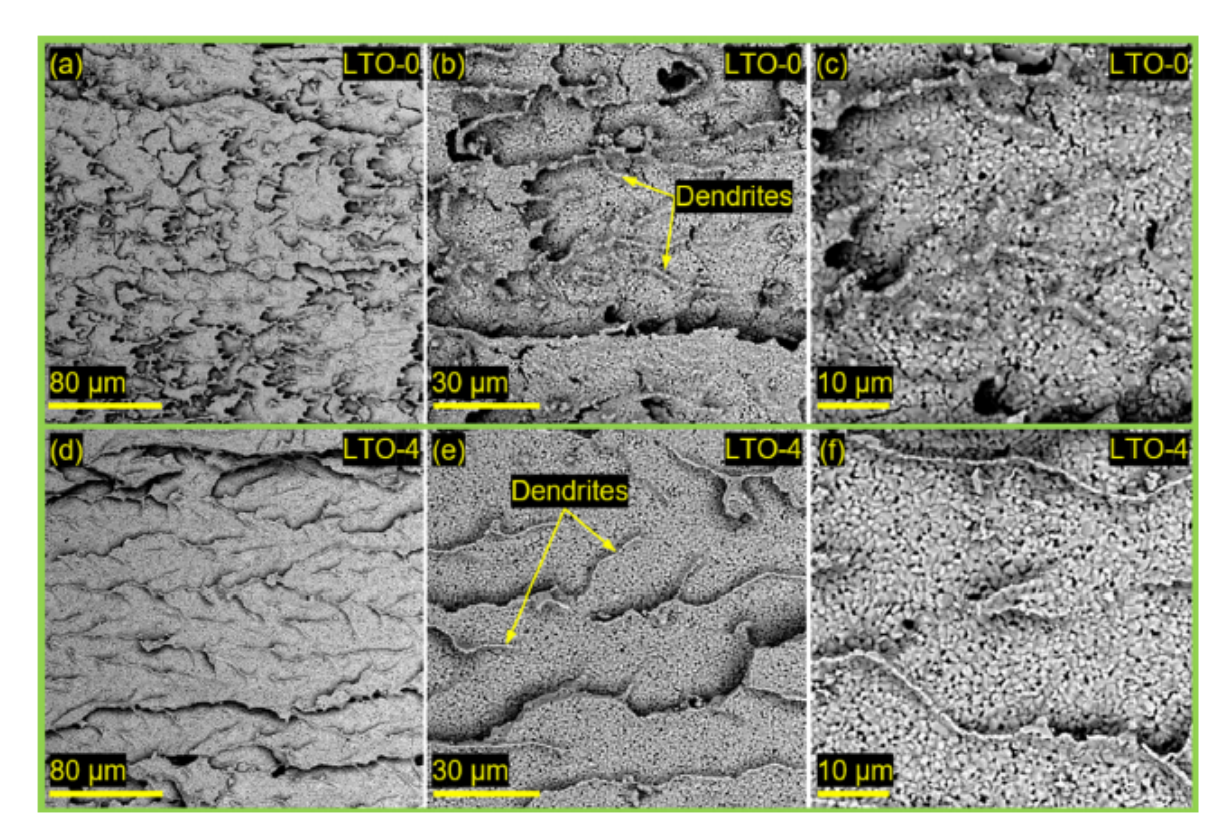


Fig. 9. SEM images at different magnifications revealing characteristics of lamella walls of (a-c) LTO-0 and (d-f) LTO-4 materials.

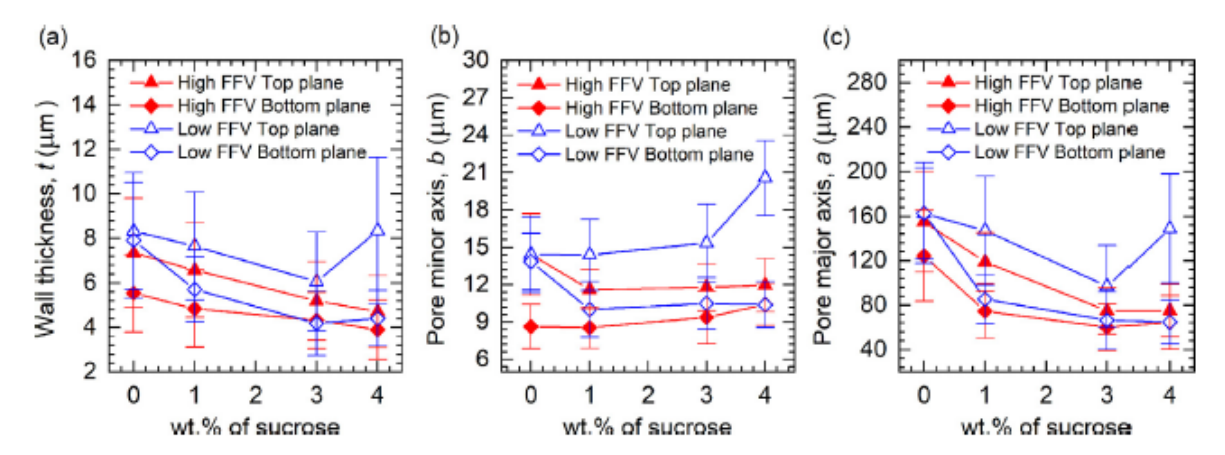


Fig. 10. Variation of (a) Lamella wall thickness, t, (b) pore minor axis, b, and (c) pore major axis, a, with sucrose content for ice-templated sintered LTO materials processed at relatively high FFV and low FFV. Blue hollow triangle and diamond represent measurements corresponding to top and bottom image planes, respectively, of materials fabricated at low FFV. Similarly, red solid triangle and diamond represent measurements corresponding to top and bottom image planes, respectively, of materials fabricated at high FFV. The error represents the standard deviation of a minimum of 50 measurements from two independent samples.

of the overall decrease in pore size (i.e., size of ice crystals) due to sucrose in aqueous LTO suspensions. All the measurements show that pore size increases with a decrease in FFV and along the growth direction of ice crystals (which is due to the decrease of FFV along that direction). Therefore, the microstructural analysis suggests that with the increase in sucrose content in LTO suspensions, overall pore size decreased. The decrease in pore size with increasing sucrose also suggests an increase in the connectivity between adjacent lamella walls.

To quantify the wall connectivity, we estimated lamellar bridge density (ρ_b), which is defined as the number of bridges that connect the adjacent lamella walls per unit area [5,24]. To estimate ρ_b from the analysis of SEM images, any connection between two adjacent walls was considered a bridge. Fig. 11 shows the variation of ρ_b with sucrose content for the materials processed at low and high FFVs. We can state that within the range of 20–35 μ m/s, the effect of FFV alone on lamel-

lar bridge density is relatively insignificant. With the increase in sucrose content in suspensions, bridge density increased significantly. For each suspension composition with sucrose and FFV regime, there is a considerable difference in bridge density between the bottom and top planes, with bridge density decreased from bottom to top. Also, for each composition and at a location in the sample (bottom or top), bridge density increased with FFV. Fig. 11 reveals that with the increase of sucrose content in suspensions, the difference of bridge density between the bottom and top planes increased significantly, with the gap appears to be comparable for both the FFV regimes. We can observe comparable bridge density values between the top plane of low FFV LTO-4 samples and the bottom plane of high FFV LTO-0 samples. Thus, the lowest bridge density in the LTO-4 materials (at low FFV) is comparable to the highest bridge density from bottom to top is directly related to the increase of bridge density from bottom to top is directly related to the increase

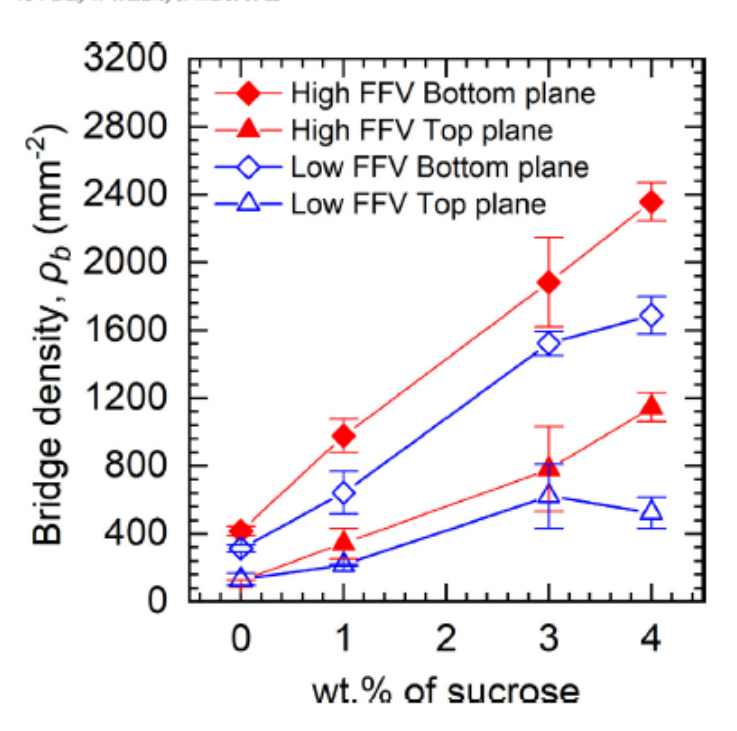


Fig. 11. Variation of lamellar bridge density (ρ_b) with sucrose content in icetemplated sintered LTO materials processed at relatively high FFV and low FFV. Blue hollow triangle and diamond represent measurements corresponding to top and bottom image planes, respectively, of materials fabricated at low FFV. Similarly, red solid triangle and diamond represent measurements corresponding to top and bottom image planes, respectively, of materials fabricated at high FFV.

of pore size along the growth direction of ice crystals. Similarly, the increase of bridge density with sucrose is related to a decrease in pore size. Bridge density estimation further supports the critical influence of sucrose in increasing wall connectivity. The effect became marked with the addition of only 4 wt.% sucrose and more prominent in combination with high FFV.

The microstructure analysis suggests that the most significant effect of sucrose in the synthesis of the ice-templated microstructure is on wall connectivity. The presence of sucrose also promoted the development of local pores. Therefore, for a given volume fraction of LTO particles in aqueous suspensions, it is possible to tailor pore size and wall connectivity in ice-templated LTO materials by carefully selecting sucrose content in the suspension and controlling FFV during the templating step. The connectivity between adjacent lamella walls is essential for the compressive load-bearing capacity of ice-templated materials, which we will discuss in the next section.

The observed microstructural changes could be related to the change in the viscosity of aqueous LTO suspensions due to sucrose. In the unidirectional solidification process, two dominant forces act on a particle present at the front of an advancing solid-liquid interface: thermomolecular force (F_r) and cryosuction (or drag) force (F_η) [3]. F_r , which is generally a repulsive force, repels the particle from the solidification front. On the other hand, F_η , the viscous drag exerted by the fluid on a particle during solidification front-particle interactions, is an attractive force that compresses the particle toward the growth front and favors engulfment. From the balance of F_η and F_r , a critical freezing front velocity $(\nu_{\rm cr})$ for a suspension is derived, above which the solidification front will completely engulf particles as [3]:

$$v_{cr} = \frac{\Delta \sigma_0 d}{3 \eta R} \left(\frac{a_0}{d} \right)^z. \quad (1)$$

 $\Delta\sigma_0$ is the mean free energy of a particle, a_0 is the average intermolecular distance in the liquid film between the particle and the solid front, d is the overall thickness of this film, η is the slurry viscosity, R is the particle radius, and z is an exponent that can vary from 1 to 5. Accord-

ing to equation (1), v_{cr} decreases with η . Thus, an increase in η tends to promote particle entrapment within solvent crystals, whereas a decrease in η tends to favor particle rejection. Particle engulfment will promote the connectivity between adjacent lamella walls and increase lamellar bridge density.

Recall that the LTO-1, LTO-3, and LTO-4 materials were fabricated from aqueous suspensions without using CTAB (cationic dispersant). Thus, it is possible that the viscosity of these suspensions (containing sucrose) was higher compared to the LTO suspensions prepared without sucrose and containing CTAB. Also, with the increasing sucrose content, the viscosity of suspensions can increase. As a result, the propensity for particle entrapment might have increased from LTO-0 to LTO-4 suspensions and hence lamellar bridge density. A separate study will be conducted on the rheological characterization of aqueous LTO suspensions prepared with and without sucrose to towards understanding the underlying mechanisms.

3.5. Compressive mechanical response

Figs. 12a and 12b show representative uniaxial stress-strain curves (up to engineering strain 0.3) of ice-templated sintered LTO materials with varying sucrose content for high and low FFV processing conditions, respectively. The inset in Fig. 12a shows the stress-strain curve for LTO-0 material. Whereas, Fig. 12c shows the variation of average maximum compressive strength (referred to here as peak stress, σ_p) with sucrose content in aqueous LTO suspensions for both high and low FFVs. The error represents the standard deviation in the strength of four independent samples. For each composition and FFV regime, four specimens were tested. All the materials exhibited a similar characteristic of compressive response with an elastic regime where stress varies linearly with strain and a stress plateau regime where stress decreases gradually with increasing strain. The stress plateau regime corresponds to the continuous brittle crushing of ice-templated porous ceramics under uniaxial compressive loading conditions [12,32].

Average σ_p (with standard deviation) of low FFV LTO-0 materials is observed to be extremely low, 3.9 \pm 0.5 MPa, and an increase in FFV from low to high FFV regime resulted in only a moderate increase of strength, 11.2 \pm 1.7 MPa. We compared the compressive strength of LTO-0 materials to other ice-templated sintered ceramics. An earlier study [12] on ice-templated alumina (Al $_2$ O $_3$, a structural ceramic) materials with porosity about 63 vol.% and lamellar morphology revealed compressive strength in the range of 40–125 MPa, indicating exceptionally low strength of LTO-0 materials compared to their porosity. LTO ceramic is a significantly weaker oxide material compared to structural ceramics [33,34], and the morphology of LTO-0 materials is highly lamellar (Fig. 5); both these factors could have contributed to reducing the compressive strength.

On the other hand, the addition of only 1 wt.% sucrose to LTO suspensions resulted in an almost five-fold (in both FFV regimes) strength increase in the LTO-1 materials. Average σ_p (with standard deviation) of low FFV LTO-1 and high FFV LTO-1 materials are 19.2 ± 1.9 MPa and 48.5 ± 4.2 MPa, respectively. With the further increase of sucrose content, strength continued to increase and increased significantly. At each composition, the strength of ice-templated sintered LTO materials increased from low FFV regime to high FFV regime, and with the increase in sucrose content, the strength gap widened. Average σ_p (with standard deviation) of low FFV LTO-3 and high FFV LTO-3 materials are 30.9 \pm 5.7 MPa and 71.6 \pm 3 MPa, respectively. Whereas, average σ_p (with standard deviation) of low FFV LTO-4 and high FFV LTO-4 materials are 41.0 ± 1.5 MPa and 80.2 ± 3.9 MPa, respectively. Therefore, the LTO-3 and LTO-4 materials exhibited approximately seven-fold and eight-fold, respectively, strength increase compared to the LTO-0 materials. Note that all the sintered materials were of comparable porosity, in the narrow range of 60-65 vol.%. However, by adding only 4 wt.% sucrose to aqueous LTO suspensions and templating the materials at relatively high FFV conditions (\sim 30 μ m/s), we were able to hamess

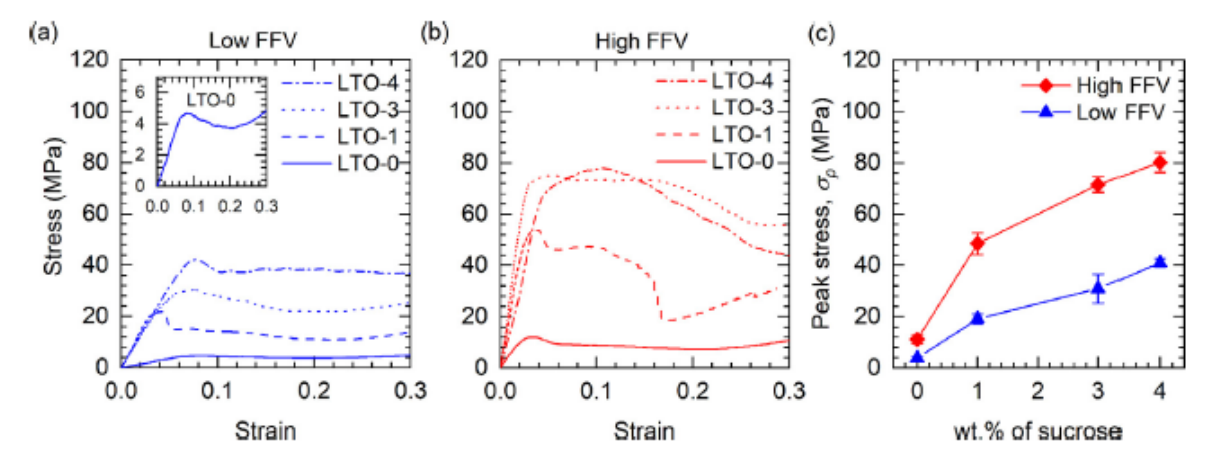


Fig. 12. Representative uniaxial compressive stress-strain curves of ice-templated sintered LTO materials with varying sucrose content for (a) low FFV ($\sim 20~\mu\text{m/s}$) and (b) high FFV ($\sim 30~\mu\text{m/s}$). Inset in (a) shows stress-strain curve for LTO-0. (c) Variation of average maximum compressive strength (σ_p) with sucrose content for high FFV (red diamond) and low FFV (blue triangle). The error represents the standard deviation in strength of four independent samples.

an unprecedented strength gain in ice-templated sintered LTO materials. Thus, the sucrose-induced microstructural modifications enabled to overcome the intrinsic weakness of LTO phase and resulted in a remarkable strength enhancement. The results strongly suggest that by adjusting sucrose content in LTO suspensions and FFV, we can tailor ice-templated sintered microstructure (pore size and wall connectivity) to develop materials with strength within a broad range of 4–80 MPa, while still maintaining the characteristic microstructural features.

Another significant benefit is that the addition of sucrose greatly enhanced the brittle crushing strength beyond peak stress (in the apparent stress plateau regime). Mainly, the LTO-3 and LTO-4 materials exhibited high compressive strength (in both FFV regimes) during the stage of continuous brittle crushing, which suggests that these materials well maintained the compressive load-bearing capacity even after the initiation of brittle fracture within the structure. Under uniaxial compressive loading, in the stress plateau regime, brittle cellular solids typically do not fail abruptly but fail by the process of progressive microfracture (i.e., graceful failure) [35,36]. During the deformation beyond the peak stress, brittle fracture in cell walls causes local failure and stress drop. However, the overall structural resistance can be maintained if there is sufficient microstructural resistance to macroscopic crack propagation. The magnitude of compressive stress and signature of the compressive stress-strain curve beyond peak stress are a direct reflection on the structural resistance. The current results strongly suggest that, particularly in the LTO-3 and LTO-4 materials, the increased connectivity between lamella walls greatly enhanced the microstructural resistance to brittle crack propagation within the templated structure and hence the materials were able to exhibit high compressive strength during continuous brittle crushing. Microstructural modifications due to sucrose not only affected strength but also failure strain. Fig. 13 shows the variation of failure strain (i.e., strain corresponding to peak stress) with the sucrose content in aqueous LTO suspensions. Except for the low FFV LTO-0 material, the general trend is that with the increasing sucrose content, failure strain increased. Therefore, with the increasing sucrose content, as the strength of the materials increased, the materials also exhibited greater elastic deformation prior to failure.

According to Gibson and Ashby models [35], compressive strength (σ) of brittle cellular solids is related to relative density (ρ_r) as

$$\frac{\sigma}{\sigma_s} \propto \rho_T$$
 (for closed – cell, brittle crushing), (2)

$$\frac{\sigma}{\sigma_{\rm S}} \propto (\rho_{\rm r})^{1.5}$$
 (for open – cell, brittle crushing), (3)

and

 $\frac{\sigma}{E_{\rm S}} \propto \left(\rho_{\rm T} \right)^3$ (for honeycomb, out - of - plane deformation, elastic buckling).

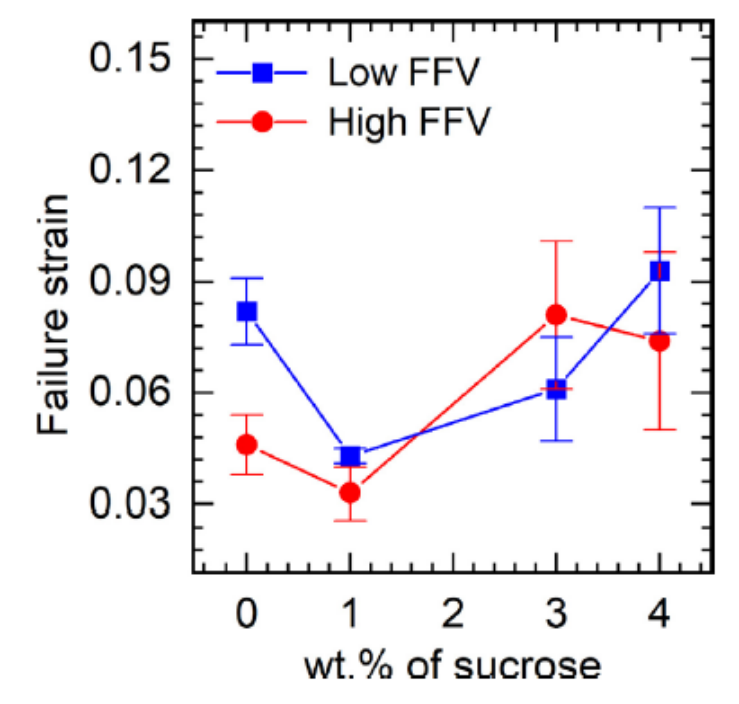


Fig. 13. Variation of failure strain (i.e., strain corresponding to peak stress) with sucrose content in aqueous LTO suspensions. The error represents the standard deviation in failure strain of four independent samples.

(4)

Here, σ_s and E_s are compressive strength and Young's modulus, respectively, of cell wall material. The semi-empirical analytical Gibson and Ashby models relate to the deformation mechanisms of cell walls and edges. For example, for the out-of-plane compressive deformation in honeycomb structure (loading direction parallel to the axis of hexagonal cells), cell walls suffer compression, i.e., experience significant axial deformation as well as shear. Ceramic cell walls will first deform elastically, but beyond a critical strain, the collapse of the walls sets the limit for maximum strength. Note that for equation (4), elastic buckling of cell walls is the strength-limiting factor in honeycombs for out-of-plane compressive deformation [35]. Strength prediction for the out-of-plane brittle failure of honeycombs (assuming defect-free cell walls) [35] well exceeded the strength prediction of closed-cell foam by brittle crushing and was thus not considered here.

Fig. 14 compares the variation of σ_p (normalized by the flexural strength of sintered LTO, 149 MPa, [33]) with ρ_r to the model predic-

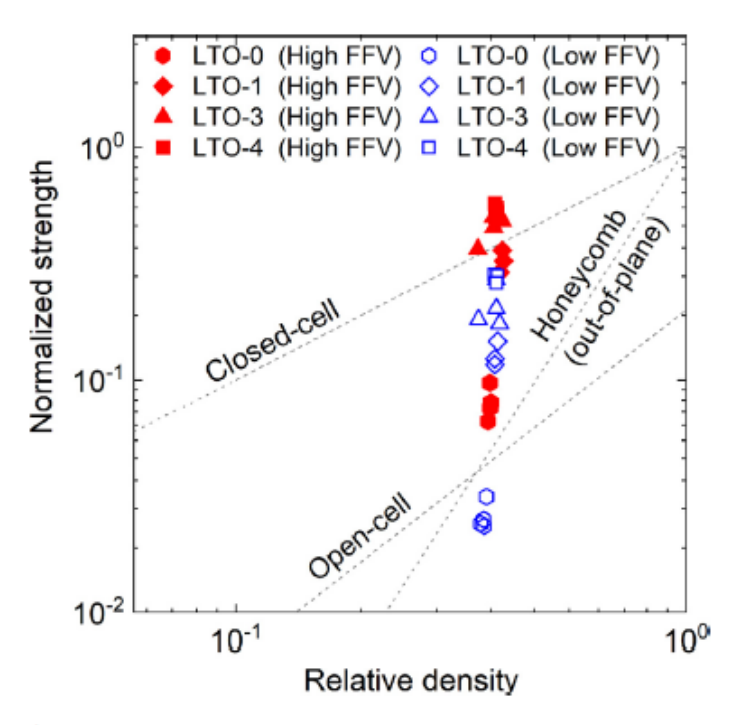


Fig. 14. Variation of normalized compressive strength of ice-templated sintered LTO materials with their relative density. The dotted lines represent the model predictions of compressive strength by Gibson and Ashby for closed-cell, open cell, and honeycomb (out-of-plane deformation) foams [46]. Solid and hollow symbols correspond to strength of materials fabricated at relatively high FFV (\sim 30 μ m/s) and low FFV (\sim 20 μ m/s).

tions (dotted lines). The measured strength values of LTO-0 materials at low FFV is observed to be relatively close to that predicted for the outof-plane deformation of honeycomb. In contrast, for high FFV strength values are moderately above the model prediction. A few other studies on ice-templated ceramics also reported similar results, where the experimental values are in a reasonable agreement with the model prediction for the out-of-plane compressive deformation of honeycomb [12,37]. An agreement with the model prediction for a honeycomb structure is reasonable considering a level of resemblance that exists between honeycomb and ice-templated porous structures. This is somewhat interesting as well since equation (4) considers elastic buckling as the strengthlimiting mechanism, which occurs in rubber type materials that are highly compliant [35]. As with the increasing sucrose content and FFV strength of ice-templated sintered LTO materials increased, the measured strength values, however, deviated significantly from the model prediction for honeycomb. For the high FFV LTO-1, LTO-3 and LTO-4 materials, the strength values are either close to or exceeded the model prediction for brittle crushing of closed-cell foam. The deviation from the model prediction for the out-of-plane deformation of honeycomb suggests a possible change in the failure mechanism or significant increase in resistance to failure in the LTO-1, LTO-3, and LTO-4 materials (i.e., materials with increased lamellar bridge density). With the increasing sucrose content, the development of intra-lamella pores (as discussed in Section 3.3) can be attributed to the increasing similarity with the model prediction for closed-cell foam. Nevertheless, with the increasing sucrose content, strength increase is a direct consequence of the increased wall connectivity.

To further substantiate the influence of wall connectivity on strength, in Fig. 15, we show the variation of maximum compressive strength with lamellar bridge density. For each composition and FFV, an average of ρ_b of top and bottom planes is used. In Fig. 15, we have also shown the variation of a dimensionless morphological parameter "m" (average of top and bottom planes) with sucrose content. Naglieri et al. [24] defined

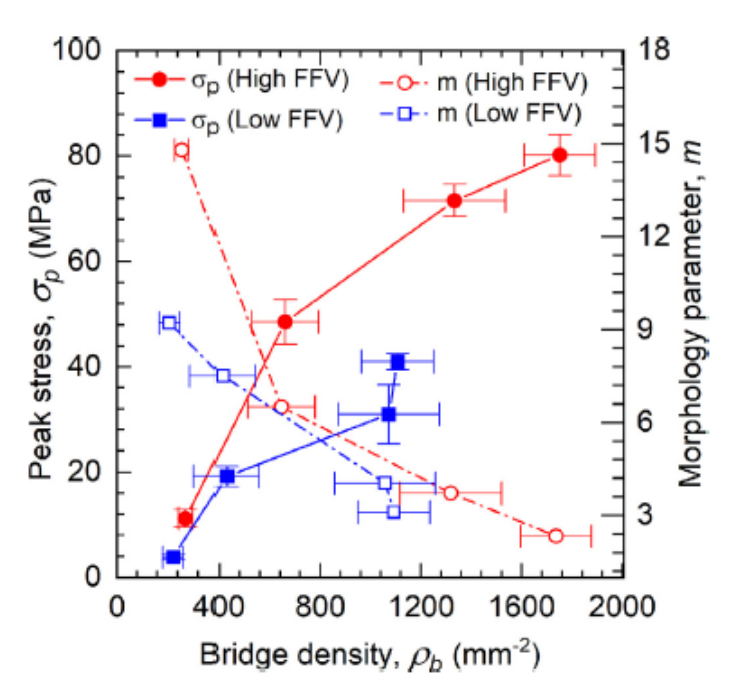


Fig. 15. Variation of average maximum compressive strength and dimensionless morphological parameter "m" with lamellar bridge density.

m as

$$m = \frac{\left(1/\rho_b\right)}{12},$$
 (5)

where ρ_b is lamellar bridge density, and λ is the wavelength (defined earlier in Section 3.4). In equation (5), $1/\rho_b$ represents the square of the spacing of the bridges, which is divided by the square of the wavelength of lamella walls. According to Naglieri et al. [24], pore morphology is lamellar for m > 5, dendritic for 1 < m < 5, and isotropic for m < 1. Morphology of the LTO-0 materials is lamellar in both FFV regimes, since m > 9. With increasing sucrose content, m decreased significantly and is about 3 for the LTO-4 materials, suggesting dendritic morphology that is consistent with the microstructural observations and bridge density estimation. Fig. 15 reveals a strong correlation between bridge density, morphology, and compressive strength. As the bridge density increased (i.e., wall connectivity) and the morphology of the materials approached toward dendritic, the compressive strength of the materials increased dramatically. Fig. 15 also provides a materials design space and suggests how sucrose content and FFV can be adjusted to tailor bridge density, morphology, and compressive strength in ice-templated ceramics.

Ice-templated porous ceramics synthesized from low solid loading suspensions contain tall, slender lamella walls. The ceramic walls are the primary structural components that carry the applied compressive load and exhibit resistance to elastic deformation [12],[32]. During elastic deformation, initiation of brittle cracking within lamella walls sets the limit for maximum fracture strength in ice-templated ceramics. Under uniaxial compression, lamella walls can experience a state of stress other than uniaxial. This is because ceramic walls in ice-templated ceramics are not rigidly clamped and under compression can exhibit lateral displacements as well, which will cause a deviation from the uniaxial state of stress. Therefore, an elastic instability can arise and cause the premature brittle failure of lamella walls, which also occurs in honeycombs for out-of-plane compressive deformation [35]. One possibility of the onset of premature brittle fracture in lamella walls from elastic instability is the buckling of the walls [12,32]. Thin lamella walls in ice-templated porous ceramics, where lamellar bridge density is negligible, are highly prone to failure by buckling. As a result, the lack of stability of the walls could be the origin of low compressive strength in LTO-0 materials. On

the other hand, with the increase in lamellar bridge density, the resistance to elastic instability in lamella walls of ice-templated LTO materials increased and hence compressive strength.

Ice-templated sintered ceramics exhibit higher compressive strength (along the growth direction of ice crystals) compared to open-cell ceramic foams having randomly oriented pores [10]. However, the strength advantage is significantly lost in the materials that are developed from low solid loading ceramic suspensions. As a result, processing methodologies that can result in strength enhancement but without reducing porosity are of significant interest. Irrespective of the final porosity, ice-templated materials synthesized from low solid loading suspensions exhibit highly lamellar morphology with thin lamella walls and low connectivity between the walls, which attribute to their poor compressive load-bearing capacity. For example, ice-templated sintered LTO materials (LTO-0) developed in this study had porosity about 65 vol.% but still exhibited very low compressive strength (~10 MPa). In this investigation, which is a first study on the development and mechanical characterization of ice-templated sintered LTO materials, we revealed that sucrose (a water-soluble additive) has a dramatic influence on microstructure and compressive strength. Although a few previous studies reported the effects of water-soluble additives on ice-templated microstructure, we thoroughly investigated the influence of sucrose content and FFV on microstructure and compressive strength and addressed the structure-property relationships. The primary effect of sucrose is that it significantly increased the connectivity between lamella walls (quantified as lamellar bridge density). However, the resultant materials still maintained the characteristic features of the ice-templated microstructure, and the change in porosity was marginal. The results revealed that sucrose content and FFV could be effectively tuned to tailor lamellar bridge density in ice-templated materials. In the sintered materials, compressive strength varied from 4 MPa in low FFV LTO-0 materials to 80 MPa in high FFV LTO-4 materials.

Moreover, in each FFV regime, materials exhibited a five-fold to eight-fold increase in compressive strength. The results revealed a direct correlation between lamellar bridge density, morphology, and compressive strength. In addition to maximum compressive strength, sucrose-induced microstructural changes also improved the load-bearing capacity in the continuous brittle crushing regime. Therefore, even when brittle fracture initiated, crack propagation through the structure became difficult due to enhanced connectivity between adjacent lamella walls.

4. Conclusions

This study developed ice-templated sintered LTO materials and investigated the influence of sucrose content in aqueous suspensions and FFV on templated microstructure and uniaxial compressive response. All the materials were synthesized from 20 vol.% aqueous LTO suspensions and developed without and with sucrose (a water-soluble additive). For the compositions with sucrose, 1, 3, and 4 wt.% (relative to the water content) sucrose was used. Materials were templated at relatively high FFV (~30 μ m/s) and low FFV (~20 μ m/s). The porosity of all the materials was in the narrow range of 60-65 vol.%, and the addition of sucrose reduced porosity by only 2 vol.%. On the other hand, the microstructural investigation revealed that sucrose had a remarkable impact on microstructure and morphology. The LTO materials templated without sucrose was of lamellar morphology with insignificant lamellar bridges. With increasing sucrose content, bridge density significantly increased, and material morphology became highly dendritic. As a result of increased connectivity between adjacent lamella walls, sintered materials exhibited a dramatic increase in compressive strength, with as high as the eight-fold increase in strength was measured. The results revealed a strong correlation between lamellar bridge density, morphology, and compressive strength. Therefore, the variation of sucrose content in aqueous suspensions and FFV provides a novel approach to significantly tailor microstructure, morphology, and compressive strength of ice-templated sintered LTO materials. While the previous studies of

directional porosity using battery electrode materials focused on ion transport and electrochemical performance benefits, this study provides some of the first insights into the process-structure-mechanical property relationships of ice-templated sintered LTO materials.

Declaration of Competing Interest

The authors declare that they have no known competing financial interests or personal relationships that could have appeared to influence the work reported in this paper.

Acknowledgments

The authors thank the US National Science Foundation (NSF) for the support of this work, via grant CMMI-1825338. TW and JM thank support through NSF REU supplement funding.

Supplementary materials

Supplementary material associated with this article can be found, in the online version, at doi:10.1016/j.mtla.2020.100901.

References

- K.L. Scotti, D.C. Dunand, Freeze casting a review of processing, microstructure and properties via the open data repository, FreezeCasting.net, Prog. Mater. Sci. 94 (2018) 243–305.
- [2] S. Deville, The lure of ice-templating: recent trends and opportunities for porous materials, Scr. Mater. 147 (2018) 119–124.
- [3] I. Nelson, S.E. Naleway, Intrinsic and extrinsic control of freeze casting, J, Mater. Res. Technol. 8 (2) (2019) 2372–2385.
- [4] S. Deville, Ice-templating, freeze casting: Beyond materials processing, J. Mater. Res. 28 (17) (2013) 2202–2219.
- [5] D. Ghosh, H. Kang, M. Banda, V. Kamaha, Influence of anisotropic grains (platelets) on the microstructure and uniaxial compressive response of ice-templated sintered alumina scaffolds, Acta Mater. 125 (2017) 1–14.
- [6] D. Ghosh, N. Dhavale, M. Banda, H. Kang, A comparison of microstructure and uniaxial compressive response of ice-templated alumina scaffolds fabricated from two different particle sizes, Ceram. Int. 42 (2016) 16138–16147.
- [7] H. Zhang, Ice templating and freeze-drying for porous materials and their applications, John Wiley & Sons, USA, 2018.
- [8] S. Deville, S. Meille, J. Seuba, A meta-analysis of the mechanical properties of ice-templated ceramics and metals, Sci. Technol Adv. Mater. 16 (4) (2015) 04350.
- [9] S. Deville, Freezing colloids: observations, principles, control, and use: applications in materials science, life science, earth science, food science, and engineering, Springer, 2017.
- [10] S. Deville, E. Saiz, R.K. Nalla, A.P. Tomsia, Freezing as a path to build complex composites, Sci 311 (5760) (2006) 515-518.
- [11] A. Lichtner, D. Roussel, D. Jauffrès, C.L. Martin, R.K. Bordia, Effect of macropore anisotropy on the mechanical response of hierarchically porous ceramics, J. Am. Ceram. Soc. 99 (3) (2016) 979–987.
- [12] M. Banda, D. Ghosh, Effects of porosity and strain rate on the uniaxial compressive response of ice-templated sintered macroporous alumina, Acta Mater. 149 (2018) 179–192.
- [13] D. Ghosh, M. Banda, N. Dhavale, H. Kang, Platelet-induced stiffening and strengthening of ice-templated Al₂O₃ scaffolds, Scr. Mater. 125 (2016) 29–33.
- [14] M. Banda, D. Ghosh, Effects of temperature and platelets on lamella wall microstructure, structural stability, and compressive strength in ice-templated ceramics, Materialia 9 (2020) 100537.
- [15] U.G. Wegst, M. Schecter, A.E. Donius, P.M. Hunger, Biomaterials by freeze casting, Philos. Trans. Royal Soc. A: Math., Phys. Eng. Sci. 368 (1917) (2010) 2099–2121.
- [16] M.M. Porter, R. Imperio, M. Wen, M.A. Meyers, J. McKittrick, Bioinspired scaffolds with varying pore architectures and mechanical properties, Adv. Funct. Mater. 24 (2014) 1978–1987.
- [17] E. Munch, E. Saiz, A.P. Tomsia, S. Deville, Architectural control of freeze-cast ceramics through additives and templating, J. Am. Ceram. Soc. 92 (2009) 1534–1539.
- [18] B.V. Babu, K.V. Babu, G.T. Aregai, L.S. Devi, B.M. Latha, M.S. Reddi, K. Samatha, V. Veeraiah, Structural and electrical properties of Li₄Ti₅O₁₂ anode material for lithium-ion batteries, Results Phys 9 (2018) 284–289.
- [19] B. Delattre, R. Amin, J. Sander, J. De Coninck, A.P. Tomsia, Y.-M. Chiang, Impact of pone tortuosity on electrode kinetics in lithium battery electrodes: study in directionally freeze-cast LiNi_{0.8}Co_{0.15}Al_{0.05}O₂ (NCA), J. Electrochem. Soc. 165 (2018) A388_A305
- [20] C. Huang, P.S. Grant, Coral-like directional porosity lithium ion battery cathodes by ice templating, J. Mater. Chem. A 6 (30) (2018) 14689–14699.
- [21] Z. Qi, G.M. Koenig Jr, A carbon-free lithium-ion solid dispersion redox couple with low viscosity for redox flow batteries, J. Power Sources 323 (2016) 97–106.
- [22] Z. Qi, G.M. Koenig Jr, Electrochemical evaluation of suspensions of lithium-ion battery active materials as an indicator of rate capability, J. Electrochem. Soc. 164 (2017) A151–A155.

[23] N.D. Dhavale, A Comparison of Microstructure and Uniaxial Compressive Response of Ice-Templated Porous Alumina Scaffolds Fabricated from Two Different Particle Sizes Master's thesis, Old Dominion University, Norfolk, VA, USA, 2016.

- [24] V. Naglieri, H.A. Bale, B. Gludovatz, A.P. Tomsia, R.O. Ritchie, On the development of ice-templated silicon carbide scaffolds for nature-inspired structural materials, Acta Mater 61 (2013) 6948–6957.
- [25] A. Kumar, K. Mohanta, D. Kumar, O. Parkash, Green properties of dry-pressed alumina compacts fabricated using sucrose as binder, Ceram. Int. 40 (2014) 6271–6277.
- [26] K. Kataoka, Y. Takahashi, N. Kijima, J. Akimoto, K.-i. Ohshima, Single crystal growth and structure refinement of Li₄Ti₅O₁₂, J. Phys. Chem. Solids 69 (5-6) (2008) 1454–1456.
- [27] S. Deville, E. Saiz, A.P. Tomsia, Ice-templated porous alumina structures, Acta Mater. 55 (2007) 1965–1974.
- [28] S. Deville, G. Bernard-Granger, Influence of surface tension, osmotic pressure and pores morphology on the densification of ice-templated ceramics, J. Eur. Ceram. Soc. 31 (2011) 983–987.
- [29] Y. Zhang, G. Tan, D. Jiao, J. Zhang, S. Wang, F. Liu, Z. Liu, L. Zhuo, Z. Zhang, S. Deville, Ice-templated porous tungsten and tungsten carbide inspired by natural wood, J. Mater. Sci. Technol. 45 (2020) 187–197.
- [30] C.M. Pekor, P. Kisa, I. Nettleship, Effect of polyethylene glycol on the microstructure of freeze-cast alumina, J. Am. Ceram. Soc. 91 (2008) 3185–3190.

- [31] C.M. Pekor, P. Kisa, I. Nettleship, Effect of polyethylene glycol on the microstructure of freeze-cast alumina, J. Am. Ceram. Soc. 91 (2008) 3185–3190.
- [32] D. Ghosh, M. Banda, S. Akurati, H. Kang, V.O. Fakharizadeh, On the brittle fracture characteristics of lamella walls of ice-templated sintered alumina scaffolds and effects of platelets, Scr. Mater. 138 (2017) 139–144.
- [33] T. Fukushima, Lithium rechargeable battery comprising a lithium titanate sintered body, Google Pat. (2015).
- [34] R.W. Rice, The compressive strength of ceramics, in: W.W. Kriegel, H. Palmour (Eds.), Ceramics in Severe Environments. Materials Science Research, vol 5, Springer, Boston, MA, 1971.
- [35] L.J. Gibson, M.F. Ashby, Cellular Solids: Structure and Properties, 2nd ed., Cambridge University Press, Cambridge, UK, 1999.
- [36] C.G. Sammis, M.F. Ashby, The failure of brittle porous solids under compressive stress states, Acta Metall. 34 (1986) 511–526.
- [37] J. Seuba, S. Deville, C. Guizard, A.J. Stevenson, Mechanical properties and failure behavior of unidirectional porous ceramics, Sci. Rep. 6 (2016) 24326.
- [38] J. Rodriguez-Carvajal, Recent advances in magnetic structure determination by neutron powder diffraction, Physica B Condens. Matter 192 (1–2) (1993) 55–69.